Nuclear Inst. and Methods in Physics Research, A 1010 (2021) 165543

Contents lists available at ScienceDirect

Nuclear Inst. and Methods in Physics Research, A

journal homepage: www.elsevier.com/locate/nima

Repurposing a low-cost commercial Si photodiode as a detector for X-ray and γ-ray spectroscopy at temperatures up to 80 °C

G. Lioliou *, M.D.C. Whitaker, S. Butera, A.M. Barnett

Space Research Group, School of Mathematical and Physical Sciences, University of Sussex, Falmer, Brighton, BN1 9QT, UK

ARTICLE INFO

Keywords:
Si p^+-i-n^+ photodiode
Hamamatsu S5973
X-ray spectroscopy
γ-ray spectroscopy

ABSTRACT

A commercial-off-the-shelf (COTS) Si p^+-i-n^+ photodiode (Hamamatsu S5973), designed for visible and infrared detection, was repurposed for use as a low-cost and readily available detector for photon counting X-ray and γ-ray spectroscopy. The detector was investigated for its spectroscopic performance, while being coupled to a custom-made charge sensitive preamplifier, under the illumination of photons with energies up to 59.54 keV. The detector-preamplifier system was subjected to temperatures from 80 °C to 20 °C. Energy resolutions (Full Width at Half Maximum, FWHM) of 0.66 keV ± 0.05 keV at 5.9 keV, 0.70 keV ± 0.04 keV at 22.16 keV, and 0.74 keV ± 0.06 keV at 59.54 keV, were achieved at 20 °C. The energy resolution deteriorated at 80 °C, reaching a value of 1.8 keV ± 0.1 keV FWHM at 59.54 keV. The results suggested that the performance, in terms of energy resolution, of the currently reported COTS Si detector was better than that achieved with certain purpose-grown wide bandgap detectors at 20 °C and 40 °C and better than that achieved with other repurposed Si detectors at 20 °C, opening new possibilities for applications for the Hamamatsu S5973 detectors and increasing the availability of low cost X-ray and γ-ray spectroscopy instrumentation.

1. Introduction

A lot of effort has been dedicated to developing purpose-grown and application-specific X-ray and γ-ray detectors. The main aim of such work is to advance the state-of-the-art X-ray and γ-ray photon counting spectroscopy instrumentation and match the requirements of each application in terms of energy resolution, photon energy range, quantum detection efficiency, temperature range of operation, and other salient features. Semiconductor radiation detectors based on Si, specifically designed and developed for X-ray photon counting spectroscopy, include lithium drifted Si (Si(Li)), Si p^+-i-n^+ photodiodes, Charge Coupled Devices (CCDs), Si Drift Detectors (SDDs), and Depleted P-Channel Field Effect Transistors (DEPFETs). Energy resolutions close to the theoretically achievable energy resolution limited by the Fano ionization statistics (= 119 eV Full Width at Half Maximum, FWHM, at 5.9 keV) have been achieved when the detectors are operated at low temperatures (≤ 20 °C); e.g. FWHM at 5.9 keV of 130 eV with Si (Li) at −173 °C [1], of 149 eV with Si p^+-i-n^+ photodiodes at −43 °C [2], of 130 eV with CCDs at −90 °C [3], of 133 eV with SDDs at 10 °C [4], and of 131 eV with DEPFETs at room temperature [5].

The development of semiconductor radiation detectors operating at high temperatures (≥ 20 °C) is dominated by the use of wide bandgap materials. A consequence of the bandgap energy of Si (1.12 eV at 300 K [6]) is the relatively high leakage current density of Si detectors, which degrades the energy resolution of the spectrometer; this is overcome by cooling the Si detectors such that they operate at low temperatures (≤ 20 °C, and sometimes near cryogenic temperatures [7]). An alternative to the use of (cooled) Si detectors is the use of wide bandgap detectors that do not suffer from high leakage current densities and can thus withstand high temperatures without a need for cooling. 4H-SiC Schottky diodes were coupled to ultra-low-noise preamplifier electronics and the spectrometer operated up to 100 °C with an energy resolution (FWHM at 5.9 keV) of 233 eV [8]. GaAs X-ray detectors have also been investigated for their performance in photon counting X-ray spectroscopy without cooling; the best experimental results were achieved with p^+-i-n^+ photodiodes employing Schottky contacts, with a reported energy resolution of 266 eV FWHM at 5.9 keV at room temperature [9]. Recently, a spectroscopic system based on a pixel CdTe detector has been successfully operated at room temperature with 472 eV FWHM at 59.54 keV [10]. GaAs p^+-i-n^+ photodiode detector based spectrometers have been operated with an energy resolution of 2.0 keV FWHM at 5.9 keV at 100 °C [11]. Better energy resolutions at 100 °C have been achieved using detectors made from wider bandgap energies than that of GaAs; energy resolutions of 1.31 keV and 1.27 keV FWHM at 5.9 keV at 100 °C have been reported using AlInP [12] and InGaP [13] detectors, respectively. Commercial-off-the-shelf (COTS) SiC photodiodes, originally intended for UV detection, have also been investigated for use as detectors for photon counting

* Corresponding author.
E-mail address: G.Lioliou@sussex.ac.uk (G. Lioliou).

https://doi.org/10.1016/j.nima.2021.165543
Received 26 April 2021; Accepted 6 June 2021
Available online 9 June 2021
0168-9002/© 2021 The Authors. Published by Elsevier B.V. This is an open access article under the CC BY license (http://creativecommons.org/licenses/by/4.0/).

X-ray [14] and γ-ray [15] spectroscopy and particle counting electron spectroscopy [16].

In addition to developing purpose-grown Si X-ray detectors, work has also been conducted on investigating the suitability of commercial Si detectors that have been originally designed for different applications, for X-ray detection. Repurposing commercial Si detectors and using them for X-ray (and γ-ray) detection provides the advantage of reduced cost. University-led CubeSat missions, radiation dosimetry, and applications requiring frequent replacements of the radiation detector are only few examples where the use of low-cost and readily available commercial Si detectors may be the only choice.

COTS Si p^+-i-n^+ photodiodes, originally not intended for radiation detection, have been adapted or repurposed for this. Examples where they have been used for radiation detection include the use of the OSRAM BPX65 Si p^+-i-n^+ photodiode for room temperature spectroscopic detection of X-ray and γ-ray photons (with a FWHM at 59.5 keV of 2.5 keV [17]) and electrons (with an average FWHM at energies up to 100 keV of 3.371 keV [18]). The Siemens SFH00206 K and Hamamatsu S2506-04 have also been investigated for X-ray and γ-ray photon counting spectroscopy, with a FWHM at 59.54 keV of 2.1 keV and 1.8 keV, respectively, at room temperature [19]. Commercial Si p^+-i-n^+ photodiodes have been used in diagnostic radiology for dosimetry; e.g. Hamamatsu S2506-02 [20], Siemens SFH205, SFH206, BPX90F, and Vishay BPW34 [21], and Hamamatsu S1223 [22].

Another COTS Si detector is the Hamamatsu S5973. It was designed for visible and infrared detection, for optical fibre communications, and photometry [23]. The S5973 has been used in time-domain fluorescence lifetime measurement systems [24], as well as to read out crystal scintillators in calorimetric electron telescope instruments [25]. Such devices have also been investigated for their radiation hardness while been irradiated by a proton beam with 24 GeV c^{-1} momentum [26]; recovery from the radiation damage was reported to be achieved by operation at increased applied reverse biases. Another application for which the S5973 has been studied previously is X-ray pulses measurements in time-resolved diffraction and scattering measurement systems [27].

Here, for the first time, the Hamamatsu S5973 detector is repurposed for use in photon counting X-ray and γ-ray spectroscopy. The detector was coupled to a custom charge sensitive preamplifier and standard onwards readout electronics. The detector was illuminated directly by photons from three radioisotope radiation sources (^{55}Fe X-ray, ^{109}Cd X-ray and γ-ray, and ^{241}Am X-ray and γ-ray), providing photons with characteristic energies up to 88.04 keV. It is important to note that the detector and preamplifier were operated uncooled at high temperatures; this is unusual for Si detectors. The detector and preamplifier were operated at temperatures between 80 °C and 20 °C. Initially, measurements of the noise contribution of the detector to the energy resolution of the spectrometer were performed. Then, X-ray and γ-ray spectra were accumulated to explore the photon counting spectroscopic performance of the detector.

The Hamamatsu S5973 Si p^+-i-n^+ photodiode had a 0.5 μm thick p^+ layer, a 10 μm thick i layer (doping density of $\sim 10^{13}$ cm^{-3}), and an n^+ layer with a doping density of $\sim 10^{18}$ cm^{-3} [28]. Its effective photosensitive area (open for illumination) was 0.12 mm^2. The detector was packaged in a TO-18 metal case [23].

2. Results and discussions

2.1. Quantum detection efficiency

The quantum detection efficiency, *QE*, of a semiconductor radiation detector in part determines the photon energy range within which it can operate effectively and the spectrum accumulation time required. It depends on the detector's structure and material; it can be calculated using the Beer–Lambert law,

$$QE = \left[\prod_m exp(-\mu_{att,m} x_m)\right]\left[1 - exp(-\mu_{abs} x_a)\right], \quad (1)$$

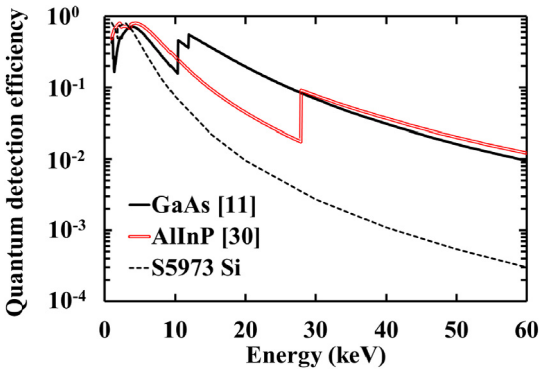

Fig. 1. Quantum detection efficiency at the open-for-illumination area of the S5973 detector (black dashed line) as a function of photon energy; the quantum detection efficiency of previously reported AlInP (red double line) [30] and GaAs (black solid line) [11] detectors is also shown for comparison. (For interpretation of the references to colour in this figure legend, the reader is referred to the web version of this article.)

where the first term accounts for the attenuation of photons within the mth top dead layer with a linear attenuation coefficient of $\mu_{att,m}$ and a thickness of x_m, and the second term accounts for the absorption of photons within the active layer with a linear absorption coefficient of μ_{abs} and a thickness of x_a. Only the area open for illumination (i.e. not covered by the contact) of the detector was considered; the top dead layer was the p^+ layer and the active layer was the i layer. The quantum detection efficiency was calculated using Eq. (1) and the linear attenuation and absorption coefficients of Si for photon energies up to 60 keV [29], and can be seen in Fig. 1. The reduction of *QE* with increasing photon energy is apparent in Fig. 1. It reduced from 0.2944 at 5.9 keV (Mn Kα) to 0.0069 at 22.16 keV (Ag Kα), and to 0.0003 at 59.54 keV (^{241}Am $\gamma_{2,0}$(Np) transition). The rapid reduction of the linear absorption coefficient of Si with increasing photon energy, and hence reduction of *QE* of Si detectors with increasing photon energy, as shown in Fig. 1, makes other semiconductor materials with larger linear attenuation coefficients the commonly preferred choice over Si for the detection of hard X-rays and γ-rays. However, it should be noted that the Hamamatsu S5973 was not designed as an X-ray or γ-ray detector, and it is relatively thin compared with most Si photodiodes designed for X-ray or γ-ray detection. For comparison, the *QE* of p^+-i-n^+ photodiodes with structures similar to the S5973, but made from semiconductor materials with large linear absorption coefficients are also presented in Fig. 1; shown in the figure are data for circular mesa (400 μm diameter) AlInP [30] and GaAs [11] p^+-i-n^+ photodiodes with 10 μm thick i layers.

2.2. X-ray and γ-ray spectroscopy

2.2.1. Noise components

The energy resolution (full width at half maximum, in energy terms), ΔE [eV], of a non-avalanche semiconductor detector X-ray or γ-ray spectrometer is composed of three noise components, the Fano noise, ΔE_{Fano}, the electronic noise, ΔE_{El}, and the incomplete charge collection noise, ΔE_{ICC} [31,32], such that

$$\Delta E = \sqrt{\Delta E_{Fano}{}^2 + \Delta E_{El}{}^2 + \Delta E_{ICC}{}^2}. \quad (2)$$

It should be noted here that Eq. (2) is valid only when the incomplete charge collection noise can be approximated by a normal distribution [33]. The Fano noise,

$$\Delta E_{Fano} = \sqrt{8 \ln 2 \omega F E}, \quad (3)$$

where ω is the average electron–hole pair creation energy, F is the Fano factor, and E is the photon energy. The total number of electron–hole pairs generated from the absorption of a photon fluctuates, and this

process induces noise to the spectrometer. The Fano noise corresponds to the fundamental resolution limit. Assuming an average electron–hole pair creation energy of 3.67 eV (for X-rays and γ-rays at 300 K [34]) and a Fano factor of 0.11 [35] for Si, the Fano noise was calculated using Eq. (3); it was calculated to increase from 47 eV at 1 keV to 367 eV at 60 keV.

The electronic noise arises from the semiconductor detector, the input JFET of the preamplifier, and their coupling. It consists of four components: white parallel noise, white series noise (including the induced gate current noise), $1/f$ noise, and dielectric noise [31].

The white parallel noise arises from the shot noise of the total leakage current, I_{tot}, flowing at the input of the preamplifier, and its equivalent noise charge (ENC) is

$$ENC_{WP} = \sqrt{\frac{A_3 I_{tot}\tau}{\mathrm{q}}} = \sqrt{B\tau}, \tag{4}$$

where A_3 is a constant depending on the type of the shaping amplifier (= 1.85 in this case), τ is the shaping time of the shaping amplifier, and q is the charge of an electron [31]. The term B is commonly used to parameterize the white parallel noise contribution. The total leakage current that gives rise to white parallel noise, $I_{tot} = 2I_D + 2I_{JFET}$, is the sum of twice the leakage current of the detector, I_D, and twice the leakage current of the preamplifier's input JFET, I_{JFET} [36].

The white series noise arises from the thermal noise of the current flowing at the channel of the input JFET of the preamplifier, and its equivalent noise charge is

$$ENC_{WS} = \frac{1}{\mathrm{q}}\sqrt{G_c A_1 \frac{\gamma}{g_m} 2\mathrm{k}TC_{tot}^2 \frac{1}{\tau}} = \sqrt{A\frac{1}{\tau}}, \tag{5}$$

where G_c is a correction factor for the induced gate current noise, A_1 is a constant depending on the type of the shaping amplifier (= 1.85 in this case), γ is a dimensionless parameter dependent on the JFET bias condition, transconductance, and its channel length, g_m is the JFET transconductance, k is the Boltzmann constant, T is the temperature in K, and C_{tot} is the total capacitance at the input of the preamplifier including the detector total capacitance, C_D, and the capacitances of the preamplifier (the input JFET capacitance, the feedback capacitance, the test capacitance, and the stray capacitances) [31]. The parameter A represents the white series noise contribution.

The $1/f$ noise arises from the flicker noise of the drain current of the preamplifier input JFET. Lastly, the dielectric noise arises from all lossy dielectrics at the input of the preamplifier including the detector and its packaging, the passivation, packaging, and dielectrics of the input JFET, and the feedback capacitance [37–39].

In addition to the Fano and electronic noise, the detector may give rise to the incomplete charge collection noise. Carrier trapping and recombination within the detector, typically at crystal imperfections (impurity atoms, vacancies, and dislocations), can lead to fluctuations in the signal charge and thus introduce noise [32]. Strictly speaking, the pulse height distribution of the incomplete charge collection noise is non-Gaussian but it may be approximated by a normal distribution when the incomplete charge collection noise is relatively small compared to the rest of the noise contributions [33].

Apart from the white parallel noise and the white series noise, all other electronic noise components are invariant with shaping time. The white parallel noise is proportional to the shaping time (Eq. (4)), whereas the white series noise is inversely proportional to the shaping time (Eq. (5)). Their quadratic sum is minimized at the optimum shaping time, τ_{opt}, where the two noise components are equal, and thus,

$$\tau_{opt} = \sqrt{\frac{A}{B}}. \tag{6}$$

2.2.2. Measurements of detector electronic noise

The contribution of the detector to the electronic noise, in terms of white parallel noise, ENC_{WP}, and white series noise, ENC_{WS}, was determined as a function of temperature.

i. Experimental procedure

The detector's leakage current and capacitance as functions of applied reverse bias of the packaged COTS Si detector were measured within the temperature range 100 °C to 20 °C. The detector was installed in a light tight and electromagnetically shielded Al enclosure. The temperature was increased to 100 °C, and then reduced in 20 °C steps with measurements made at each temperature. The temperature was controlled using a TAS Micro LT climatic cabinet. Dry N_2 was used to purged continually the climatic cabinet to maintain its relative humidity ≤ 5% and thus eliminate any humidity related effects. The leakage current measurements were performed using a Keithley 6487 Picoammeter/Voltage Source. The capacitance was measured with an HP Multi Frequency LCR meter employing a test signal of 50 mV rms magnitude and 1 MHz frequency. In both cases (leakage current and capacitance measurements), applied reverse biases up to 100 V in magnitude (1 V step size) were investigated. It is important to note that because the detector was packaged at the time of the measurements, the measurements of leakage current and capacitance included contributions from the packaging of the detector as well that from the detector itself.

ii. Results

The leakage current of the packaged detector at 20 °C and within the temperature range from 100 °C to 20 °C, can be seen in Fig. 2. The values presented included the leakage current of the photodiode detector itself (arising from the bulk and potentially from the surface) as well as the leakage current of the TO-18 package.

The total leakage current reduced from 4.086 nA ± 0.009 nA at 100 °C to 0.8 pA ± 0.4 pA at 20 °C, at 100 V applied reverse bias. The leakage current of the packaged detector, at 20 V applied reverse bias (the operating condition used for accumulation of the radiation spectra, see Section 2.2.3 and 2.2.4) reduced from 3.767 nA ± 0.009 nA at 100 °C to a value lower than the noise floor of the measuring system (± 0.4 pA) at 20 °C. The white parallel noise contribution of the packaged detector to the energy resolution of the X-ray and γ-ray spectrometer, at the operating conditions of the spectrometer used in the radiation measurements, was calculated using Eq. (4)); it was 72 e^- rms ± 4 e^- rms at 80 °C (20 V applied reverse bias; 0.5 μs shaping time) and ≤ 10 e^- rms at 20 °C (20 V applied reverse bias; 2 μs shaping time). The calculated white parallel noise arising from the packaged detector at 100 °C (20 V applied reverse bias; 0.5 μs shaping time) was 209 e^- rms ± 10 e^- rms; such a high value was prohibitive for the operation of the X-ray and γ-ray spectrometer, as such radiation spectroscopy was limited to temperatures ≤ 80 °C.

For comparison purposes, previously reported state-of-the-art wide bandgap III–V photodiode detectors contributed ~10 e^- rms of white parallel noise at 30 °C, under their normal operating conditions: 13 e^- rms for a 10 μm thick i layer GaAs p^+-i-n^+ photodiode [36], ≤ 8 e^- rms for a 5 μm thick i layer InGaP p^+-i-n^+ photodiode [40], and 6 e^- rms for a 10 μm thick i layer AlInP p^+-i-n^+ photodiode [30]. The white parallel noise associated with the very low leakage currents of some state-of-the-art wide bandgap semiconductor radiation detectors can be extremely low (< 1 e^- rms at 27 °C for ultra-low leakage current SiC detectors employing Schottky contacts, [8,41]).

It should be noted that the part of the leakage current that arises from the bulk of the photodiode detector is directly proportional to the photodiode's area, and the part that arises from the surface of the photodiode detector is directly proportional to the photodiode's circumference. As such, the total leakage current may be suppressed by keeping the device size relatively small, as is the case for the currently reported COTS Si detector which has an active area of 0.12 mm^2. Relatively low leakage current densities are required for large area X-ray

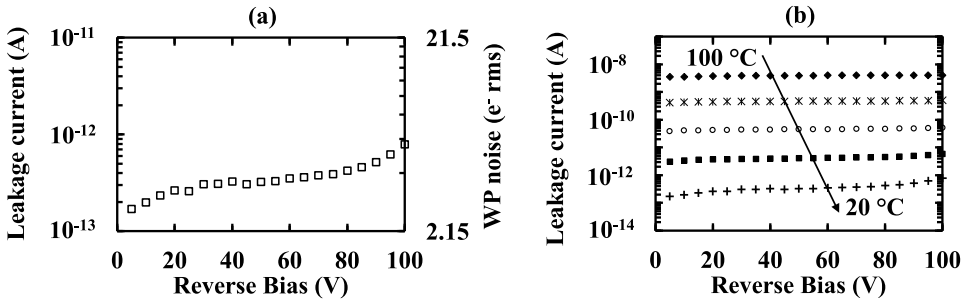

Fig. 2. Leakage current of the packaged detector as a function of applied reverse bias (a step size of 5 V is shown for clarity) at: (a) 20 °C, and (b) across the temperature range 100 °C to 20 °C: 100 °C (filled diamonds); 80 °C (stars); 60 °C (open circles); 40 °C (filled squares); 20 °C (+ symbols). The white parallel, WP, noise arising from the leakage current at 20 °C, at 2 μs shaping time, is also shown for (a).

detectors; this can be achieved using wide bandgap materials. Examples of semiconductor detectors with large areas operating without cooling include 4H-SiC X-ray detectors (e.g. 1.2 mm^2 [42]), CdTe X-ray and γ-ray detectors (e.g. 0.56 mm^2 [10]), and diamond X-ray and γ-ray detectors (4 mm^2 [43]). The total capacitance of the packaged detector at 20 °C, and also across the temperature range from 100 °C to 20 °C, can be seen in Fig. 3. It included the depletion layer capacitance of the photodiode detector itself as well as the capacitance of the TO-18 package.

The total capacitance at 20 °C reduced from 1.994 pF ± 0.006 pF at 0 V applied reverse bias to 1.500 pF ± 0.005 pF at 100 V applied reverse bias. The reduction of the total capacitance at each temperature occurred as the applied reverse bias increased in magnitude up to 20 V and remained stable for further reverse biases increases, up to 100 V, as is shown in Fig. 3(b), suggesting full depletion (and maximum quantum detection efficiency) at 20 V. The temperature dependence of the total capacitance of the packaged detector was more prominent at low applied reverse biases; it reduced from 6.49 pF ± 0.01 pF at 100 °C to 1.994 pF ± 0.006 pF at 20 °C, at 0 V. However, the total capacitance was temperature invariant as the applied reverse bias increased in magnitude; this is shown in Fig. 3(b) for 20 V and 100 V applied reverse bias. Assuming that the packaging capacitance was invariant with applied reverse bias (this was confirmed by separate measurements made using a device of the same type with the bond wires removed), the temperature dependence of the total capacitance at low applied reverse biases was attributed to the temperature dependence of the photodiode's depletion layer capacitance at low applied reverse biases (low applied electric fields). This may be explained by the limited extension of the depletion layer at high temperatures at low reverse biases. A thin region around the depletion layer with ionized dopants at high temperatures, preventing the extension of the depletion layer at low reverse biases, might be the cause. The dopants may not have enough thermal energy at low temperatures and thus they remain non-ionized, allowing the extension of the depletion layer even at low reverse biases.

The white series noise contribution of the packaged detector to the energy resolution of the X-ray and γ-ray spectrometer, at the operating conditions of the spectrometer, was calculated using Eq. (5); it was 19.18 e^- rms ± 0.07 e^- rms at 80 °C (20 V applied reverse bias; 0.5 μs shaping time) and 8.67 e^- rms ± 0.03 e^- rms at 20 °C (20 V applied reverse bias; 2 μs shaping time). Since the capacitance of the packaged detector remained constant at 20 V, within the investigated temperature range, the reduction of the white series noise as the temperature decreased from 80 °C to 20 °C was due to the difference in the shaping time used at each temperature. A different shaping time was chosen for the X-ray and γ-ray spectra accumulated at 80 °C and 20 °C; in general for radiation spectrometers the optimum shaping time at each temperature may differ, as is suggested by Eq. (6), depending on the corresponding white parallel and white series noise contributions.

2.2.3. X-ray and γ-ray spectra

i. Experimental procedure

The photon counting spectroscopic performance of the COTS Si detector was investigated by obtaining X-ray and γ-ray spectra. ^{55}Fe radioisotope X-ray spectra, ^{109}Cd radioisotope X-ray and γ-ray spectra, and ^{241}Am radioisotope X-ray and γ-ray spectra were accumulated at different temperatures.

The Si detector was coupled to a low noise, single-channel charge-sensitive preamplifier (CSP). The CSP was of a custom design; it had the feedback resistor and the external circuit to reset the preamplifier eliminated [44]. It employed an n type JFET, InterFET 2N4416, as its input transistor. The connection between the Si detector and the input JFET was such that the JFET operated in a slightly forward biased condition, thus providing a discharge path for the feedback capacitor. The detector-preamplifier system was installed in a TAS Micro LT climatic cabinet for temperature control. The output of the preamplifier was amplified and shaped by an ORTEC 572 A shaping amplifier with a semi-Gaussian pulse and six available shaping times (0.5 μs, 1 μs, 2 μs, 3 μs, 6 μs, and 10 μs). The digitalization of the pulses was then performed with an ORTEC EASYMCA 8k multichannel analyser (MCA). Both ORTEC instruments operated at room temperature.

The detector was directly illuminated by photons from the three sources of radiation in turn (an ^{55}Fe radioisotope X-ray source, a ^{109}Cd radioisotope X-ray and γ-ray source, and an ^{241}Am radioisotope X-ray and γ-ray source) and spectra were accumulated in each case. The capsules containing each of the sources were made of stainless steel and had 250 μm thick Be windows. The ^{55}Fe X-ray radioisotope source, emitting characteristic lines of Mn Kα (5.9 keV) and Mn Kβ (6.49 keV) [45], had an activity of 99 MBq. The ^{109}Cd X-ray and γ-ray radioisotope source, emitting characteristic lines of Ag Kα_1 (22.16 keV), Kα_2 (21.99 keV), Kβ (24.9 keV), Lα (2.98 keV) X-rays, and the 88.03 keV γ-ray line [46], had an activity of 179 MBq. Lastly, the ^{241}Am X-ray and γ-ray radioisotope source, emitting characteristic lines of Np Lα (13.76 keV and 13.95 keV), Lβ (ranging from 16.11 keV to 17.99 keV), and Lγ (ranging from 20.78 keV to 21.49 keV) X-rays [47], and the 26.3 keV, 33.2 keV, 43.4 keV, and 59.54 keV γ-ray lines [48], had an activity of 299 MBq.

The X-ray and γ-ray spectra were accumulated with the detector and preamplifier both operated at the same temperature. The maximum temperature, 80 °C, was limited by the leakage current of the detector (Fig. 2); the leakage current at 100 °C was prohibitively high for the operation of the X-ray and γ-ray spectrometer. Initially, ^{55}Fe radioisotope X-ray spectra were accumulated at each investigated temperature (80 °C to 20 °C with 20 °C steps) as functions of applied reverse bias (0 V, 20 V, and 100 V) at all available shaping times. This allowed an insight into the noise contributions which set the energy resolution of the spectrometer and as a result, enabled the optimum (for best FWHM at 5.9 keV) available shaping time and applied reverse bias at each temperature to be identified. Subsequently, the ^{109}Cd radioisotope X-ray and γ-ray spectra and the ^{241}Am radioisotope X-ray and γ-ray

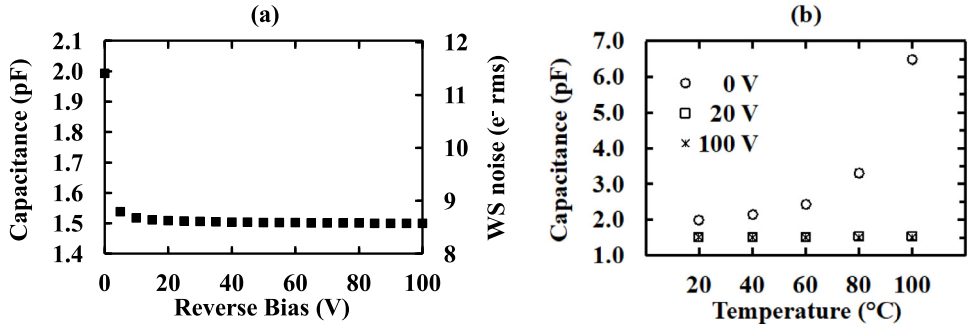

Fig. 3. Capacitance of the packaged detector, i.e. including both the detector die and its packaging, as a function of (a) applied reverse bias (a step size of 5 V is shown for clarity) at 20 °C and (b) temperature at 0 V (open circles), 20 V (open squares), and 100 V (stars) applied reverse bias. The white series, WS, noise arising from the capacitance at 20 °C, at 2 μs shaping time, is also shown.

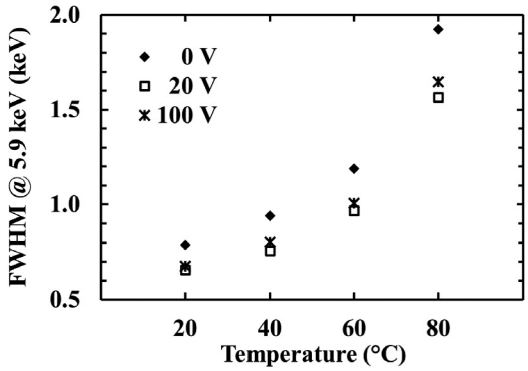

Fig. 4. Best FWHM at 5.9 keV as a function of temperature, at each investigated applied reverse bias: 0 V (filled diamonds); 20 V (open squares); 100 V (stars).

spectra were obtained at only the optimum available shaping time and applied reverse bias at each temperature. The live time limit of the spectra was chosen to provide sufficiently good counting statistics; it was 120 s for the ^{55}Fe radioisotope X-ray spectra, 3600 s for the ^{109}Cd radioisotope X-ray and γ-ray spectra, and 25,200 s for the ^{241}Am radioisotope X-ray and γ-ray spectra.

ii. ^{55}Fe radioisotope X-ray spectra: results and discussion

The detected photopeak in each ^{55}Fe X-ray spectrum was the combined photopeaks of the Mn Kα (5.9 keV) and Mn Kβ (6.49 keV) characteristic X-ray emissions. The Mn Kα and Kβ contributions were deconvolved through analysis and the FWHM at 5.9 keV was established. The summation of two Gaussians (one for Mn Kα, one for Mn Kβ) was fitted to the combined photopeak; the characteristic energies, the relative emission ratio [45] and quantum detection efficiency of the detector at the two characteristic X-ray emissions were considered for the computation of the two Gaussians. The MCA charge scale of each spectrum was energy calibrated using the position (channel number) of the 0 keV noise peak of the CSP and the position of the fitted Mn Kα photopeak. The FWHM at 5.9 keV was then deduced for each of the 72 ^{55}Fe X-ray spectra (18 spectra at each temperature, thus providing every combination of applied reverse bias and shaping time). The best FWHM at 5.9 keV at each investigated applied reverse bias (at the optimum available shaping time) as a function of temperature can be seen in Fig. 4. The best FWHM at 5.9 keV (i.e. that at the optimum available shaping time) at each temperature improved as the applied reverse bias increased in magnitude from 0 V to 20 V and then, either remained stable (at 20 °C) or deteriorated (at 40 °C, 60 °C, and 80 °C) as the applied reverse bias further increased in magnitude from 20 V to 100 V. The noise contributions dependent upon the detector applied reverse bias are the white parallel noise (Eq. (4), total leakage current of detector, I_D), the white series noise (Eq. (5), total capacitance of detector, C_D), and the incomplete charge collection noise. The improvement of the FWHM at 5.9 keV as the applied reverse bias increased in magnitude from 0 V to 20 V was attributed to both the reduction of the capacitance of the detector (Fig. 3) and to the potential improvement of the charge transport and collection within the detector at an increased internal electric field leading to a reduction of the incomplete charge collection noise. The detector capacitance, and thus the white series noise, did not reduce as the applied reverse bias was further increased from 20 V to 100 V (Fig. 3). Instead, the increase of the detector leakage current at increased applied reverse biases, at temperatures ≥ 40 °C, resulted in a deterioration of energy resolution as the applied reverse bias was increased in magnitude from 20 V to 100 V.

Example ^{55}Fe radioisotope X-ray spectra can be seen in Fig. 5. Partial collection of charge created in the non-active layers of the detector (within one diffusion length from the depletion region) resulted in the low energy tailing at the left hand side of the combined Mn Kα and Mn Kβ X-ray photopeak. The counts of the 0 keV noise peak of the preamplifier were limited by setting the MCA low energy cut-off channel number at > 0 keV (e.g. at 1 keV for the spectra shown in Fig. 5(a)) a few seconds after establishing its position at the start of the accumulation; the right hand side of the tail of the zero energy noise peak, which was above the threshold set, was still visible.

The ^{55}Fe X-ray spectra with the best FWHM at 5.9 keV (occurred at 2 μs shaping time), as obtained with the COTS Si detector based spectrometer at each investigated applied reverse bias, at 20 °C, can be seen in Fig. 5(a). The FWHM at 5.9 keV improved from 0.79 keV ± 0.05 keV at 0 V to 0.66 keV ± 0.05 keV at 20 V (0.68 keV ± 0.05 keV at 100 V) applied reverse bias. The count rate at the Mn Kα peak (number of counts contained within the Gaussian fitted to the Mn Kα X-ray peak divided by the spectra accumulation time) was calculated in order to investigate potential incomplete charge collection; it increased from 3720 counts s^{-1} ± 60 counts s^{-1} at 0 V to 3920 counts s^{-1} ± 60 counts s^{-1} at 20 V and to 4010 counts s^{-1} ± 60 counts s^{-1} at 100 V. The count rate at the Mn Kα peak remained stable (within uncertainties) as the applied reverse bias increased in magnitude from 20 V to 100 V; this was expected since the detector was fully depleted at 20 V, but it also suggested that the improvement of the charge transport with increased applied reverse bias, beyond 20 V, was insignificant. Thus, it was concluded that the optimum applied reverse bias for the COTS Si detector, to achieve the best energy resolution as well as to ensure relatively high charge collection efficiency, was 20 V. The ^{55}Fe X-ray spectra with the best FWHM at 5.9 keV at 80 °C and 20 °C (20 V applied reverse bias), can be seen in Fig. 5(b). The energy resolution improved from 1.6 keV ± 0.1 keV FWHM at 5.9 keV at 80 °C to 0.66 keV ± 0.05 keV FWHM at 5.9 keV, at 20 °C. The ENC at 5.9 keV was calculated; it reduced from 182 e$^-$ rms ± 13 e$^-$ rms at 80 °C to 76 e$^-$ rms ± 6 e$^-$ rms at 20 °C.

The FWHM at 5.9 keV obtained with the detector operated at 20 V applied reverse at all investigated temperatures and shaping times can

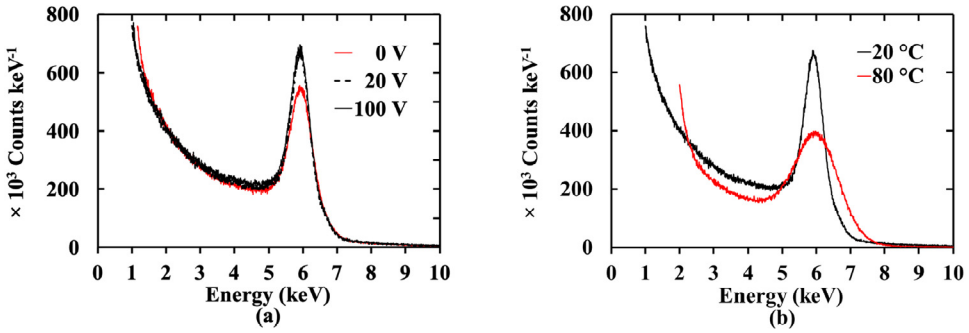

Fig. 5. ^{55}Fe radioisotope X-ray spectra accumulated (a) at 20 °C and the optimum available shaping time (2 μs) and applied reverse biases of 0 V (solid red line), 20 V (dashed black line), and 100 V (solid black line); and (b) at 80 °C (20 V; 0.5 μs; FWHM at 5.9 keV = 1.6 keV ± 0.1 keV; red line) and 20 °C (20 V; 2 μs; FWHM at 5.9 keV = 0.66 keV ± 0.05 keV; black line). In each case, the photopeak is the combination of the characteristic Mn Kα and Kβ X-ray emissions from the ^{55}Fe radioisotope X-ray source. (For interpretation of the references to colour in this figure legend, the reader is referred to the web version of this article.)

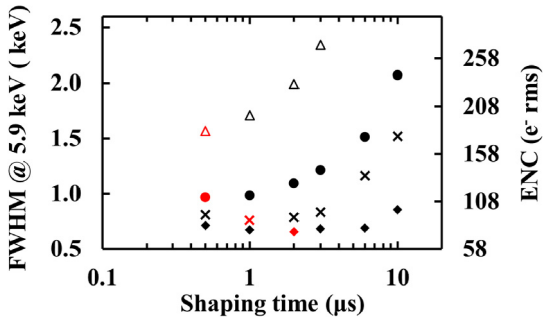

Fig. 6. FWHM at 5.9 keV, at 20 V applied reverse bias as a function of shaping time, within the investigated temperature range: 80 °C (open triangles); 60 °C (filled circles); 40 °C (× symbols); 20 °C (filled diamonds). The optimum available shaping time at each temperature is marked in red. (For interpretation of the references to colour in this figure legend, the reader is referred to the web version of this article.)

be seen in Fig. 6. Although the optimum shaping time (to achieve the best energy resolution) can be calculated using Eq. (6), if the available shaping time cannot be infinitely continuously adjusted, the optimum shaping time may be different from the best available shaping time. Among the available shaping times on the shaping amplifier employed in the measurements, the best available shaping time was 0.5 μs at 80 °C and 60 °C, 1 μs at 40 °C, and 2 μs at 20 °C. The reduction of the total leakage current of the spectroscopic system (detector and input JFET) with reduced temperature resulted in the observed lengthening of the best available shaping time as the spectrometer was cooled from 80 °C to 20 °C. According to the measurements of the contribution of the packaged detector to the electronic noise (Section 2.2.2), it contributed 72 e^- rms ± 4 e^- rms of white parallel noise and 19.18 e^- rms ± 0.07 e^- rms of white series noise at 80 °C (20 V applied reverse bias; 0.5 μs shaping time). Although the packaged detector was not the only source of white parallel and white series noise, these findings along with Eq. (6) suggested that a shaping time shorter than 0.5 μs at 80 °C may result in an energy resolution better than 1.6 keV ± 0.1 keV FWHM at 5.9 keV. The packaged detector contributed ≤ 10 e^- rms of white parallel noise and 8.67 e^- rms ± 0.03 e^- rms of white series noise at 20 °C (20 V applied reverse bias; 2 μs shaping time).

The deterioration of the energy resolution (FWHM at 5.9 keV) at long shaping times and at all temperatures (see Fig. 6) was initially solely attributed to the white parallel noise contribution from the total leakage current being present in the spectrometer. The possible effects of other contributions to the broadening of the photopeak at long shaping times was then investigated at 20 °C. Two parameters, the count rate within the fitted Mn Kα and the count rate beyond 9 keV, were calculated and their dependency on shaping time was explored. The count rate within the Mn Kα photopeak was first calculated from the total number of counts within the fitted Gaussian at the Mn Kα (5.9 keV) photopeak divided by the live time (120 s); this is shown in Fig. 7(a) as a function of shaping time. The count rate at 5.9 keV remained constant at all investigated shaping times (= 3400 counts s^{-1} ± 360 counts s^{-1} at 0.5 μs and 3350 counts s^{-1} ± 520 counts s^{-1} at 10 μs).

Pulse pile up effects occur at relatively high counting rates and sufficiently long shaping times, where two or more events may be interpreted as a single event and thus result in spectral artefacts [49]. The effect of pulse pile-up events where the combined energy was greater than would lay within the Mn Kα-Kβ photopeak was explored. The count rate (total number of counts over the spectrum accumulation time) corresponding to counts with energies > 9 keV was recorded at 20°C (20 V applied reverse bias) as a function of shaping time; this is shown in Fig. 7(b). The count rate at detected energies beyond 9 keV increased from 48 counts s^{-1} at 0.5 μs to 870 counts s^{-1} at 10 μs. This suggested pulse pile-up at long shaping times (> 3 μs at 20 °C). This effect however did not contribute to the degradation of the energy resolution (FWHM at 5.9 keV) at long shaping times. The best FWHM at 5.9 keV achieved at each investigated temperature can be seen in Fig. 8. The total noise present reduced by 143 e^- rms ± 15 e^- rms as the temperature reduced from 80 °C to 60 °C, by 70 e^- rms ± 10 e^- rms as the temperature reduced from 60 °C to 40 °C, and by 44 e^- rms ± 7 e^- rms as the temperature reduced from 40 °C to 20 °C.

The FWHM at 5.9 keV achieved using previously reported purpose-grown wide bandgap pixel detector based spectrometers, employing the same type of charge-sensitive preamplifier electronics, is also shown in Fig. 8, for comparison purposes. These detectors (GaAs with a 10 μm thick i layer [50]; AlInP with a 6 μm thick i layer [51]; InGaP with a 5 μm thick i layer [52]) were square mesa p^+-i-n^+ photodiodes with areas of 200 μm × 200 μm (0.04 mm^2). Even though the energy resolutions achieved using the COTS Si detector were inferior compared to those using the purpose-grown wide bandgap detectors at temperatures > 60 °C (see Fig. 8), this was not the case at 20 °C and 40 °C. The spectrometer employing the Si detector had the same FWHM at 5.9 keV (in energy terms, within uncertainties) as that employing the purpose-grown GaAs detector [50] and it had better FWHM at 5.9 keV than those employing the purpose-grown AlInP and InGaP detectors [51,52]. It is important to note that all of the spectrometers used the same type of Si input JFET in their CSPs, and that the performance of this input transistor largely limits the performance of the wide bandgap spectrometers at high temperatures; the necessity of wide bandgap input JFETs for spectroscopy preamplifiers employing wide bandgap detectors has been previously noted [31]. Nevertheless, the results obtained with the COTS Si detector are important — they show that such

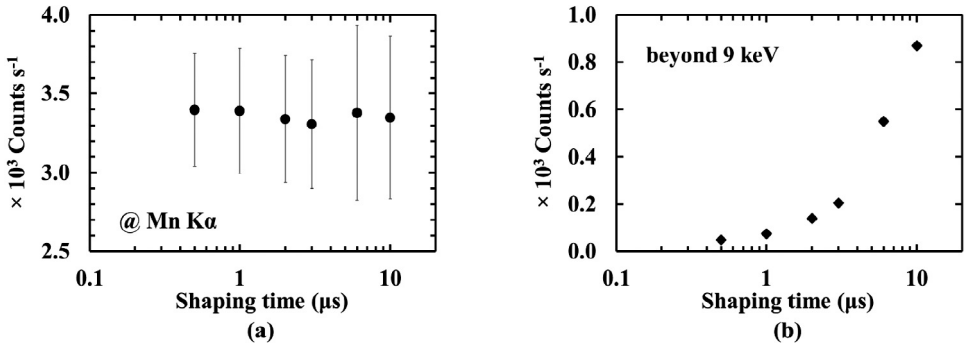

Fig. 7. (a) Count rate within the fitted Mn Kα Gaussian and (b) count rate beyond 9 keV, of the ^{55}Fe X-ray spectra accumulated with the Si COTS detector, as a function of shaping time, at 20 °C and at 20 V applied reverse bias.

a device can be used at hotter temperatures than has been previously considered possible and that, at least in certain circumstances, a COTS Si detector can outperform (in energy resolution terms) some custom wide bandgap detectors at modestly elevated (≤ 40 °C) temperatures. This is primarily a consequence of the smaller average electron–hole pair creation energy of Si cf. the wider bandgap materials, as will be shown below. This highlights the need to tailor the detector material to the specific temperature regime to which the detector will be subjected as has been previously noted in earlier works on wide bandgap X-ray detectors [53,54]: the detector physicist should select a material which has the smallest electron–hole pair creation energy possible yet also a bandgap wide enough that noise arising from the leakage current does not significantly degrade the energy resolution achievable. The exact relationship between electron–hole pair creation energy and bandgap is still a matter of contemporary interest [55].

It is informative to compare the energy resolutions of the COTS Si detector and those of the reference wide bandgap detectors in terms of total ENC (in e$^-$ rms) present in each spectrometer, since the electron–hole pair creation energy, ω, of the four semiconductor materials differ ($\omega_{AlInP} > \omega_{InGaP} > \omega_{GaAs} > \omega_{Si}$) at each temperature [13,34,56,57], in addition to their different bandgap, E_g, energies ($E_{gAlInP} > E_{gInGaP} > E_{gGaAs} > E_{gSi}$) at each temperature [6,58,59]. The ENC at 20 °C was 66 e$^-$ rms ± 2 e$^-$ rms for GaAs [50], 65 e$^-$ rms ± 3 e$^-$ rms for AlInP [51], 67 e$^-$ rms ± 3 e$^-$ rms for InGaP [52], and 76 e$^-$ rms ± 6 e$^-$ rms for Si. At this temperature, each of the spectrometers employing a wide bandgap detector (GaAs, AlInP, or InGaP) had the same ENC, and it was better (lower) than that of the spectrometer employing the COTS Si detector. The effect of the larger electron–hole pair creation energies of the wide bandgap materials (cf. that of Si) is thus made plain. At 80 °C, the ENC was 112 e$^-$ rms ± 3 e$^-$ rms for GaAs [50], 97 e$^-$ rms ± 4 e$^-$ rms for AlInP [51], 93 e$^-$ rms ± 3 e$^-$ rms for InGaP [52], and 182 e$^-$ rms ± 13 e$^-$ rms for Si; at this higher temperature, the benefit of the wider bandgaps of the GaAs, AlInP, and InGaP detectors outweighs the materials' greater electron–hole pair creation energies. It should be noted that whilst spectrometers employing other detectors have been reported with better energy resolutions when operated at ≈ 20 °C (e.g. 136 eV FWHM at 5.9 keV at 20 °C for Si drift detectors [60]); 131 eV FWHM at 5.9 at room temperature for Si DEPFETs [5]; 266 eV at 5.9 keV at 23 °C for GaAs Schottky photodiodes [9]) those detectors were coupled to significantly different readout electronics and thus the performance of those spectrometers cannot be directly compared with the spectrometers using the COTS Si, AlInP, InGaP, and GaAs detectors previously discussed as a proxy for performance of the detectors themselves. It is also informative to compare the energy resolution (FWHM at 5.9 keV) achieved with the COTS Si detector with that for a previously reported spectrometer employing a repurposed COTS 4H-SiC p-n photodiode detector, originally intended for UV detection [15].

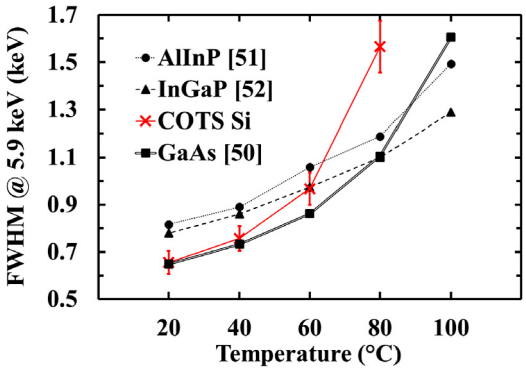

Fig. 8. Best FWHM at 5.9 keV as a function of temperature achieved with the X-ray spectrometer employing the COTS Si detector (× symbols) and previously reported spectrometers using AlInP [51] (filled circles), InGaP [52] (filled triangles), and GaAs [50] (filled squares) detectors. Each of the spectrometers use the same type of preamplifier electronics. The lines are guides to the eyes only. (For interpretation of the references to colour in this figure legend, the reader is referred to the web version of this article.)

The energy resolution (FWHM at 5.9 keV) achieved with the COTS 4H-SiC detector improved from 2.30 keV at 80 °C to 1.66 keV at 20 °C. Although the bandgap energy, E_g, of 4H-SiC (= 3.27 eV [61]) is wider than that of Si, the performance of the COTS 4H-SiC detector based spectrometer was inferior compared to that of the COTS Si detector based spectrometer, in terms of energy resolution, up to 80 °C. This was, in part, attributed to their different thicknesses and, thus, different capacitances. The COTS 4H-SiC detector had an epilayer thickness of only 5.15 μm and the capacitance measurements suggested that only a portion of it was depleted under the operating conditions of the spectra accumulation [15]; the capacitance of the packaged COTS 4H-SiC detector was 2.7 pF [15], whereas the capacitance of the COTS Si detector was 1.5 pF. As a result, the COTS 4H-SiC detector contributed higher white series noise to the energy resolution of the spectrometer cf. that of the COTS Si detector. However, even when excluding the higher ENC of the 4H-SiC detector based spectrometer compared to that of the COTS Si detector spectrometer (e.g. at 80 °C the ENC was 135 e$^-$ rms for the COTS 4H-SiC and 182 e$^-$ rms for the COTS Si), the energy resolution, in energy terms, achieved with the COTS Si detector based spectrometer was better than that achieved with the COTS 4H-SiC detector based spectrometer. This was attributed to the smaller average electron–hole pair creation energy of Si cf. 4H-SiC (= 7.28 eV [62]) and is another example which highlights the effect of the large average electron–hole pair creation energy of wide bandgap materials to the achieved energy resolution of spectrometers based on detectors made of these materials.

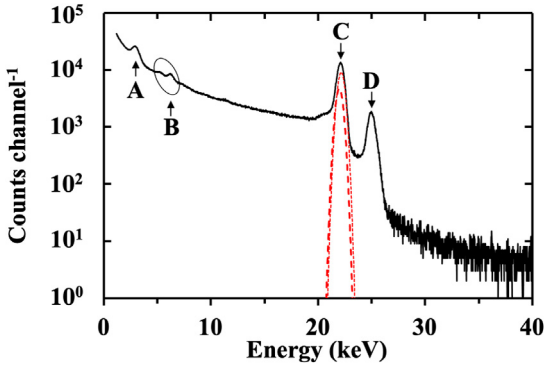

Fig. 9. ^{109}Cd X-ray and γ-ray spectrum accumulated at 20 °C (20 V reverse bias and 2 μs shaping time; FWHM at 22.16 keV = 0.70 keV ± 0.04 keV; black line). The major peaks identified are: (A) ^{109}Cd Ag Lα; (B) Cr Kα and Fe Kα capsule fluorescence; (C) ^{109}Cd Ag Kα_1 and Kα_2 (combined); (D) ^{109}Cd Ag Kβ. The Gaussians fitted at the Ag Kα_1 and Kα_2 peaks are also shown (red square dotted and red dashed lines, respectively). (For interpretation of the references to colour in this figure legend, the reader is referred to the web version of this article.)

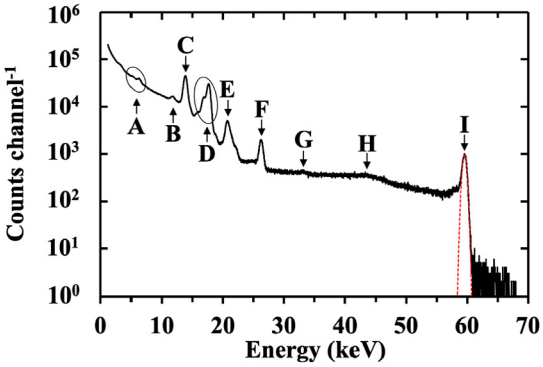

Fig. 10. ^{241}Am X-ray and γ-ray spectrum accumulated at 20 °C (20 V reverse bias; 2 μs shaping time; FWHM at 59.54 keV = 0.74 keV ± 0.06 keV; black line). The major peaks identified are: (A) Cr Kα and Fe Kα capsule fluorescence; (B) Si escape peak from ^{241}Am Np Lα photons; (C) ^{241}Am Np Lα; (D) ^{241}Am Np Lβ and Si escape peak from ^{241}Am Np Lβ photons (combined); (E) ^{241}Am Np Lγ; (F) ^{241}Am 26.3 keV γ-ray; (G) ^{241}Am 33.2 keV γ-ray; (H) ^{241}Am 43.4 keV γ-ray; (I) ^{241}Am 59.54 keV γ-ray. The Gaussians fitted at the 59.54 keV γ-ray peak is also shown (red square dotted line). (For interpretation of the references to colour in this figure legend, the reader is referred to the web version of this article.)

iii. ^{109}Cd and ^{241}Am X-ray and γ-ray spectra: results and discussion

The COTS Si detector was then illuminated with photons from a ^{109}Cd radioisotope X-ray and γ-ray source and an ^{241}Am radioisotope X-ray and γ-ray source, in turn.

The ^{109}Cd X-ray and γ-ray spectrum accumulated at 20 °C is presented in Fig. 9. The characteristic emission lines of the ^{109}Cd radioisotope X-ray and γ-ray source were the Ag Kα_1 (22.16 keV), Kα_2 (21.99 keV), Kβ (24.9 keV), and Lα (2.98 keV) X-ray emissions, and the γ-ray emissions at 88.03 keV [46], however, due to the low quantum detection efficiency at 88.03 keV and the live time limit set for the ^{109}Cd X-ray and γ-ray spectra, the 88.03 keV γ-ray peak was not formed in the spectra, for this reason for clarity, the spectrum is shown up to 40 keV only. The main photopeak in each ^{109}Cd X-ray and γ-ray spectrum was formed by the combination of the Ag Kα_1 (22.16 keV) and Kα_2 (21.99 keV) emissions; this combined peak (peak C in Fig. 9) was deconvolved by fitting Gaussian peaks representing the Ag Kα_1 and Kα_2 contributions. The two Gaussians were calculated taking into account the relative emission rate of the photons and the relative quantum detection efficiency of the detector (Fig. 1) at these energies. The position (centroid channel number) of the Ag Kα_1 and that of the zero energy noise peak were used to energy calibrate the MCA charge scale. The counts of the zero energy noise peak were limited by setting the MCA low energy cut-off at an energy > 0 keV (e.g. 2.9 keV at 80 °C and 1.2 keV at 20 °C). The FWHM at 22.16 keV was recorded following the MCA charge scale energy calibration; it improved from 1.8 keV ± 0.2 keV at 80 °C (shaping time, τ, = 0.5 μs) to 0.70 keV ± 0.04 keV at 20 °C (τ = 2 μs). It should be noted that the FWHM at 22.16 keV achieved at high temperatures using previously reported purpose-grown wide bandgap pixel detector spectrometers (having the same type of CSP electronics) was better compared to that achieved using the COTS Si detector spectrometer. The FWHM at 22.16 keV at 100 °C was 1.63 keV ± 0.06 keV for GaAs [50], 1.58 keV ± 0.08 keV for AlInP [51], and 1.32 keV ± 0.06 keV for InGaP [52], whereas a ^{109}Cd X-ray and γ-ray spectrum could not be accumulated using the COTS Si detector at this elevated temperature.

In addition to the combined Ag Kα_1 (22.16 keV) and Kα_2 (21.99 keV) photopeak, the Ag Lα peak (peak A) and the Ag Kβ peak (peak D) were also apparent in the spectra (see Fig. 9). X-ray fluorescence peaks (Fe Kα = 6.4 keV; Cr Kα = 5.4 keV) from the stainless steel encapsulation of the radioisotope were also apparent in the spectra (peak B at Fig. 9).

The ^{241}Am X-ray and γ-ray spectrum accumulated at 20 °C is presented in Fig. 10. The characteristic emission lines of the ^{241}Am radioisotope X-ray and γ-ray source were the Np Lα (at various energies from 13.76 keV to 13.95 keV), Np Lβ (16.11 keV to 17.99 keV), Np Lγ (20.78 keV to 21.49 keV) X-rays and the γ-rays at 26.3 keV, 33.2 keV, 43.4 keV, and 59.54 keV [47,48]. The ^{241}Am 59.54 keV γ-ray peak was fitted with a Gaussian peak. The position (centroid channel number) of the ^{241}Am 59.54 keV γ-ray peak and that of the zero energy noise peak were used to energy calibrate the MCA charge scale. Similarly to the ^{109}Cd X-ray and γ-ray spectra, the counts of the zero energy noise peak of the ^{241}Am X-ray and γ-ray spectra were limited by setting the MCA low energy cut-off at an energy > 0 keV (e.g. 2.9 keV at 80 °C and 1.2 keV at 20 °C). The FWHM at 59.54 keV improved from 1.8 keV ± 0.1 keV at 80 °C (τ = 0.5 μs) to 0.74 keV ± 0.06 keV at 20 °C (τ = 2 μs). Although an ^{241}Am X-ray and γ-ray spectrum could not be accumulated at 100 °C with the COTS Si detector, this was not the case when using purpose-grown wide bandgap pixel detector spectrometers (having the same type of CSP electronics). The FWHM at 59.54 keV at 100 °C was 1.65 keV ± 0.08 keV for GaAs [50], 1.57 keV ± 0.08 keV for AlInP [51], and 1.34 keV ± 0.06 keV for InGaP [52]. Better energy resolutions were achieved with purpose-grown wide bandgap detectors at 100 °C compared to that achieved with the currently reported COTS Si detector at 80 °C. Similarly to the FWHM at 5.9 keV (Fig. 8), the energy resolution at 59.54 keV achieved with the COTS Si detector was limited at high temperatures by its bandgap energy and relatively high leakage current.

The characteristic emission lines of the ^{241}Am radioisotope X-ray and γ-ray source were all apparent in the spectrum shown in Fig. 10: Np Lα (labelled C), Np Lβ (labelled D), Np Lγ (labelled E) X-rays, as well as the γ-rays at 26.3 keV (labelled F), 33.2 keV (labelled G), 43.4 keV (labelled H), and 59.54 keV (labelled I). As was the case for the ^{109}Cd X-ray spectra, X-ray fluorescence photons (Fe Kα, 6.4 keV; Cr Kα 5.4 keV) from the stainless steel encapsulation of the radioisotope is also visible in Fig. 10 (labelled A). Even though detector self-fluorescence peaks (Si Kα at 1.74 keV and Kβ at 1.84 keV) were not visible in the ^{241}Am X-ray and γ-ray spectra, Si Kα and Kβ escape peaks associated with the Np Lα and Lβ X-rays were formed; these were labelled B and D, respectively. Counts beyond the 59.54 keV γ-ray peak in the spectrum shown in Fig. 10 were the result of pulse pile up.

The FWHM at 22.16 keV and 59.54 keV achieved at 80 °C (20 V; 0.5 μs), 60 °C (20 V; 0.5 μs), 40 °C (20 V; 1 μs), 20 °C (20 V; 2 μs) can be seen in Fig. 11. A degraded energy resolution at the highest energy (59.54 keV) compared to that at 22.16 keV, would be attributed to the Fano noise (see Eq. (3)) and, potentially, to incomplete charge collection noise, since both are photon energy dependent [63]. The

Fano noise, calculated using Eq. (3), was 223 eV (26 e^- rms) at 22.16 keV and 365 eV (42 e^- rms) at 59.54 keV. The remainder from the subtraction (in quadrature) of the Fano noise from the total noise is the combined contribution of the electronic and (if any) incomplete charge collection noise (see Eq. (2)). The average among the two energies calculated combined contribution (summed in quadrature) of the electronic noise and (if any) incomplete charge collection noise was 210 e^- rms ± 1 e^- rms (rms error) at 80 °C, reducing to 76 e^- rms ± 1 e^- rms (rms error) at 20 °C. These results suggested the absence of detectable incomplete charge collection noise and the presence of 210 e^- rms ± 1 e^- rms at 80 °C and 76 e^- rms ± 1 e^- rms at 20 °C of electronic noise. Additionally, the FWHM achieved at the two energies (22.16 keV and 59.54 keV) was the same, within uncertainties, at each temperature, as can be seen from Fig. 11, even though there was an additional 289 eV (34 e^- rms) Fano noise at 59.54 keV compared to that at 22.16 keV. As such, the Fano noise contribution was insignificant compared to the electronic noise contribution for the currently reported COTS Si detector based spectrometer.

The reduction of the total noise (ENC) as the temperature reduced by 20 °C was calculated. The total noise at 22.16 keV reduced by 162 e^- rms ± 26 e^- rms as the temperature reduced from 80 °C to 60 °C, by 93 e^- rms ± 13 e^- rms as the temperature reduced from 60 °C to 40 °C, and by 63 e^- rms ± 12 e^- rms as the temperature reduced from 40 °C to 20 °C. Similarly, the total noise at 59.54 keV reduced by 170 e^- rms ± 13 e^- rms as the temperature reduced from 80 °C to 60 °C, by 70 e^- rms ± 11 e^- rms as the temperature reduced from 60 °C to 40 °C, and by 64 e^- rms ± 4 e^- rms as the temperature reduced from 40 °C to 20 °C.

The FWHM at 22.16 keV and 59.54 keV achieved using a previously reported COTS SiC detector spectrometer (having the same type of CSP) [15] is also shown in Fig. 11, for comparison purposes. The energy resolutions (in energy terms) achieved with the COTS Si detector were superior compared to those using the wide bandgap COTS 4H-SiC detector, up to 80 °C, whereas spectra were accumulated using the COTS 4H-SiC detector at 100 °C, as opposed to using the COTS Si detector. The total ENC (in e^- rms) present in each spectrometer was then compared, since the electron–hole pair creation energy of 4H-SiC (= 7.28 eV [62]) was larger than that of Si. Considering the ENC as deduced from the ^{109}Cd X-ray and γ-ray spectra, the total noise in the COTS 4H-SiC detector based spectrometer was higher (97 e^- rms [15]) compared to that in the COTS Si detector based spectrometer (82 e^- rms ± 5 e^- rms) at 20 °C. This was attributed to the higher capacitance (and white series noise contribution) of the COTS 4H-SiC detector than that of the COTS Si detector; the COTS 4H-SiC detector was thinner than the COTS Si detector and only partially depleted under the normal operating conditions of the spectrometer [15]. It should be noted that the difference of the ENC present in the two spectrometers (82 e^- rms ± 5 e^- rms for the COTS Si detector and 97 e^- rms for the COTS 4H-SiC detector) was less significant compared to their difference of the energy resolution (FWHM at 22.16 keV) in energy terms at 20 °C (0.70 keV ± 0.04 keV for the COTS Si detector and 1.66 keV for the COTS 4H-SiC detector); this was a consequence of the smaller electron–hole pair creation energy of Si cf. 4H-SiC. The ENC at 80 °C was 210 e^- rms ± 20 e^- rms for COTS Si detector and 135 e^- rms for COTS 4H-SiC detector [15]. Concluding, the benefit of the smaller electron–hole pair creation energy of Si cf. 4H-SiC outweighs the materials' narrower bandgap, up to 80 °C.

The energy resolutions achieved using the Hamamatsu S5973 detector (FWHM at 59.54 keV of 1.8 keV ± 0.1 keV at 80 °C and 0.74 keV ± 0.06 keV at 20 °C) were better than those achieved using other repurposed (for X-ray and γ-ray detection) Si detectors, e.g. 2.5 keV (OSRAM BPX65 [17]), 2.1 keV (Siemens SFH00206 K [19]) and 1.8 keV (Hamamatsu S2506-04 [19]) FWHM at 59.5 keV at room temperature. It is informative to also compare the results obtained with the detector to those previously reported for purpose-grown detectors. The best energy resolutions reported for purpose-grown X-ray and γ-ray detectors for uncooled operation (≥ 20 °C) at 59.54 keV include a 487 eV FWHM at 59.54 keV at 23 °C achieved with a GaAs p^+-i-n^+ photodiode (40 μm thick ultrapure epitaxial planar layer) employing Au/Pt/Ti Schottky contacts [9] and 472 eV FWHM at 59.54 keV at 20 °C achieved with a CdTe photodiode employing Au/Ti/Al Schottky contacts [10].

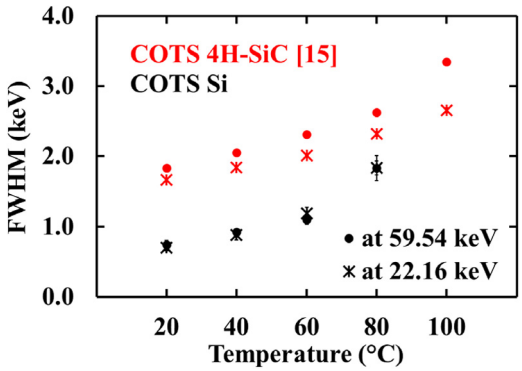

Fig. 11. FWHM at 59.54 keV (filled circles) and at 22.16 keV (stars) as a function of temperature achieved with the spectrometer employing the COTS Si detector (black symbols) and the previously reported spectrometer using 4H-SiC [15] (red symbols). (For interpretation of the references to colour in this figure legend, the reader is referred to the web version of this article.)

Although the performance achieved with the repurposed COTS Si detector is modest compared to that of the best detectors tailor made for X-ray and γ-ray detection, the results are still remarkable: the detector was designed for visible and infrared detection yet it has been shown to function has a photon counting spectroscopic detector of X-ray and γ-rays at temperatures ≤ 80 °C. Si photodiodes for X-ray and γ-ray spectroscopy have not been reported operating at such temperatures previously.

3. Conclusions

A photon counting X-ray and γ-ray spectrometer employing a repurposed COTS Si detector (Hamamatsu S5973, originally intended for visible and infrared detection) has been demonstrated to function at temperatures up to 80 °C. This is the first demonstration of this type of photodiode being used for X-ray and γ-ray spectroscopy, and the first demonstration of a Si photodiode operating uncooled in an X-ray spectrometer at temperatures significantly hotter than 20 °C; previously only wide bandgap photodiodes have been demonstrated to be capable of operation in that temperature regime.

Initially, the white parallel and white series noise contributions of the detector to the energy resolution of the spectrometer were determined. Under the normal operating conditions of the spectrometer (ensuring maximum quantum detection efficiency, best energy resolution, good charge transport), the detector (including its package) contributed 72 e^- rms ± 4 e^- rms at 80 °C and ≤ 10 e^- rms at 20 °C white parallel noise, whereas its series noise contribution was lower: 19.18 e^- rms ± 0.07 e^- rms at 80 °C and 8.67 e^- rms ± 0.03 e^- rms at 20 °C. The white parallel noise of the detector at 100 °C (209 e^- rms ± 10 e^- rms) was prohibitive for the operation of the X-ray and γ-ray spectrometer, and thus spectroscopic measurements with the detector were limited to ≤ 80 °C.

The detector was coupled to custom-made CSP and directly illuminated by photons from radioisotope radiation sources (^{55}Fe, ^{109}Cd, and ^{241}Am). The best energy resolutions (FWHM) at the maximum investigated temperature (80 °C) was 1.6 keV ± 0.1 keV at 5.9 keV, 1.8 keV ± 0.2 keV at 22.16 keV, and 1.8 keV ± 0.1 keV at 59.54 keV. The energy resolution was better at lower temperatures: at 20 °C it was 0.66 keV ± 0.05 keV at 5.9 keV, 0.70 keV ± 0.04 keV at 22.16 keV, and 0.74 keV ± 0.06 keV at 59.54 keV. This performance was achieved at

a detector reverse bias of 20 V and a shaping time of 0.5 μs at 80 °C and 2 μs at 20 °C.

Analysis of the noise within the spectroscopic system suggested that the energy resolutions were better when the detector was reverse biased at 20 V cf. 0 V due to a lower white series noise contribution from the detector and, possibly, reduction of incomplete charge collection noise. It was found that increased white parallel noise resulted in the deterioration of the energy resolution as the applied reverse bias was increased from 20 V to 100 V at temperatures ≥ 40 °C. The ^{55}Fe X-ray spectra accumulated at long shaping times (> 3 μs at 20 °C) suffered from pulse pile-up events (with a resultant energy greater than would lay within the Mn Kα-Kβ photopeak). There was no contribution of the pulse pile-up to the FWHM at 5.9 keV, since the count rate within the Mn Kα photopeak was found to be constant within the investigated shaping times. The shortest shaping time available on the shaping amplifier used in this study was 0.5 μs; consideration of the relative contributions of white parallel and white series noise suggested that an even shorter shaping time (i.e. < 0.5 μs) might result in an improved energy resolution at high temperatures (e.g. 80 °C).

Analysis of the energy resolution of the spectrometer at the two highest energies (22.16 keV and 59.54 keV), at all investigated temperatures, suggested the absence of detectable incomplete charge collection and the insignificant contribution of the Fano noise, up to 59.54 keV, when the detector was reverse biased at 20 V. The dominant source of noise of the currently reported COTS Si detector based spectrometer was the electronic noise; its contribution reduced from 210 e^- rms ± 1 e^- rms at 80 °C to 76 e^- rms ± 1 e^- rms at 20 °C.

The energy resolution of the COTS Si detector based spectrometer was compared with that achieved with previously reported X-ray and γ-ray spectrometers and conclusions were drawn. The results showed that a similar or an even better energy resolution (FWHM at 5.9 keV, in energy terms) was achieved with the COTS Si detector based spectrometer cf. previously reported purpose-grown wide bandgap pixel detector spectrometers (all employing the same CSP electronics), including GaAs [50], AlInP [51], and InGaP [52] detectors, up to 40 °C. The smaller average electron–hole pair creation energy of Si cf. the wider bandgap materials was proved beneficial at modestly elevated temperatures. However, the energy resolutions (FWHM at 5.9 keV, 22.16 keV, and 59.54 keV) achieved using the COTS Si detector were inferior compared to those using the purpose-grown wide bandgap detectors, reported in refs. [50–52] at temperatures ≥ 80 °C; the (narrow) bandgap energy of Si limited its spectroscopic performance (i.e. degraded its energy resolution) at high temperatures.

Comparisons of the performance (energy resolution in energy terms) of the COTS Si detector and a previously reported COTS 4H-SiC detector [15], intended for UV detection, when both were coupled to identical CSP electronics, highlighted again the effect of the larger electron–hole pair creation energies of the wide bandgap materials (cf. that of Si) and the benefit of that of Si; the energy resolution (FWHM at 5.9 keV, 22.16 keV, and 59.54 keV) of the COTS Si detector based spectrometer was superior to the energy resolution of the COTS 4H-SiC detector based spectrometer at ≤ 80 °C. Although the capacitance of the COTS 4H-SiC detector was higher than that of the COTS Si detector, the total ENC (in e^- rms) present in the COTS Si detector based spectrometer was larger than that in the COTS 4H-SiC spectrometer at ≥ 80 °C, due to the narrower bandgap of Si cf. that of 4H-SiC [15].

Although not coupled to the same electronics, the energy resolution achieved with the currently reported COTS Si detector (Hamamatsu S5973) was compared to that achieved using different previously reported COTS Si detectors. The OSRAM BPX65 [17], the Siemens SFH00206 K [19], and the Hamamatsu S2506-04 [19], have all been previously investigated for their performance in X-ray and γ-ray photon counting spectroscopy at room temperature. The energy resolutions achieved with those other COTS Si detectors were inferior to that achieved using the Hamamatsu S5973 detector. This was partially attributed to the low noise CSP electronics used here.

The energy resolutions achieved here were not as good as the best reported so far for X-ray and γ-ray photon counting spectrometers using purpose-made detectors and ultra-low noise electronics. The best energy resolution spectrometers operating at ≈ 20 °C and at relatively soft X-ray photon energies (≤ 10 keV) have employed Si detectors (e.g. Si drift detectors [60] and DEPFETs [5]). Operation at a higher photon energy regime (> 10 keV) and/or higher temperature regime (≥ 20 °C) benefits from the use of different semiconductor materials; the best energy resolutions reported for purpose-made X-ray and γ-ray detectors for uncooled operation achieved with a GaAs p^+-i-n^+ photodiode [9] and a CdTe photodiode [10].

The energy resolution (at the required temperature range of operation) is not the only characteristic of an X-ray and γ-ray photon counting spectrometer that leads the selection of the appropriate detector. A high quantum detection efficiency, at the specific photon energy regime to which the detector will be subjected, may be the primary requirement for certain applications (e.g. at environments with a paucity of photons). The detector in these situations should thus be tailored with the appropriate material and structure; semiconductor materials with relatively large linear attenuation coefficients are usually preferred over Si for the detection of hard X-rays and γ-rays (see Fig. 2). Finally, the radiation hardness of the detector can play a major role in its selection, especially for applications where the detector is subjected to intense radiation environments. Detector degradation (and thus a reduced lifetime) due to radiation damage can be overcome by employing detectors with increased radiation hardness; semiconductor materials such as GaAs [64] and SiC [63] suffer less from radiation damage compared to Si [7].

In conclusion, it has been demonstrated here that the COTS Si detector (Hamamatsu S5973) can be used for X-ray and γ-ray photon counting spectroscopy at elevated temperatures higher than had been previously supposed to be possible for Si detectors. In addition, the energy resolutions achieved at modestly elevated temperatures (≤ 40 °C) were superior compared to those using some wide bandgap detectors that were tailor-made for high temperature X-ray and γ-ray detection. Although the detector employed was originally intended for visible and infrared detection it may still be the preferred choice for use in low-cost X-ray and γ-ray spectroscopy instrumentation in certain applications.

CRediT authorship contribution statement

G. Lioliou: Formal analysis, Data curation, Writing - original draft, Writing - review & editing, Visualization. **M.D.C. Whitaker:** Methodology, Software, Validation, Formal analysis, Investigation, Data curation. **S. Butera:** Methodology, Validation, Formal analysis, Investigation, Data curation. **A.M. Barnett:** Conceptualization, Methodology, Validation, Formal analysis, Investigation, Resources, Data curation, Writing - original draft, Writing - review & editing, Visualization, Supervision, Project administration, Funding acquisition.

Declaration of competing interest

The authors declare the following financial interests/personal relationships which may be considered as potential competing interests: A.M. Barnett reports financial support was provided by Science and Technology Facilites Council. A.M. Barnett reports financial support was provided by Leverhulme Trust.

Acknowledgements

This work was in part supported by the Science and Technology Facilities Council, United Kingdom, through grants ST/R001804/1 and ST/T000910/1 (University of Sussex, A M B, PI). A.M.B. acknowledges funding from the Leverhulme Trust, United Kingdom, in the form of a 2016 Philip Leverhulme Prize.

References

[1] K. Tsuji, J. Injuk, R. Van Grieken, X-Ray Spectrometry: Recent Technological Advances, John Wiley & Sons, Chichester, 2004.

[2] T. Pantazis, J. Pantazis, A. Huber, R. Redus, The historical development of the thermoelectrically cooled X-ray detector and its impact on the portable and hand-held XRF industries, X-Ray Spectrom. 39 (2010) 90–97.

[3] K. Koyama, et al., X-ray Imaging spectrometer (XIS) on board suzaku, Publ. Astron. Soc. Japan 59 (2007) S23–S33.

[4] G. Bertuccio, M. Ahangarianabhari, C. Graziani, D. Macera, Y. Shi, A. Rachevski, I. Rashevskaya, A. Vacchi, G. Zampa, N. Zampa, P. Bellutti, G. Giacomini, A. Picciotto, C. Piemonte, A silicon drift detector-CMOS front-end system for high resolution X-ray spectroscopy up to room temperature, J. Instrum. 10 (2015) P01002.

[5] N. Wermes, L. Andricek, P. Fischer, M. Harter, S. Herrmann, M. Karagounis, R. Kohrs, H. Kruger, G. Lutz, P. Lechner, I. Peric, M. Porro, R. Richter, H. Soltau, L. Struder, M. Trimpl, J. Ulrici, J. Treis, New results on DEPFET pixel detectors for radiation imaging and high energy particle detection, Proc. IEEE Nucl. Sci. Symp. 1 (2003) 325–330.

[6] W. Bludau, A. Onton, W. Heinke, Temperature dependence of the band gap of silicon, J. Appl. Phys. 45 (1974) 1846–1848.

[7] A.F. Abbey, P.J. Bennie, M.J.L. Turner, B. Altieri, S. Rives, Cooling out the radiation damage on the XMM-Newton EPIC MOS CCDs, Nucl. Instrum. Methods Phys. Res. A 513 (2003) 136–142.

[8] G. Bertuccio, S. Caccia, D. Puglisi, D. Macera, Advances in silicon carbide X-ray detectors, Nucl. Instrum. Methods Phys. Res. A 652 (2011) 193–196.

[9] A. Owens, M. Bavdaz, A. Peacock, A. Poelaert, H. Andersson, S. Nenonen, H. Sipila, L. Tröger, G. Bertuccio, High resolution X-ray spectroscopy using GaAs arrays, J. Appl. Phys. 90 (2001) 5376–5381.

[10] M. Sammartini, M. Gandola, F. Mele, B. Garavelli, D. Macera, P. Pozzi, G. Bertuccio, X–γ-ray spectroscopy with a CdTe pixel detector and SIRIO preamplifier at deep submicrosecond signal-processing time, IEEE Trans. Nucl. Sci. 68 (2021) 70–75.

[11] G. Lioliou, M.D.C. Whitaker, A.M. Barnett, High temperature GaAs X-ray detectors, J. Appl. Phys. 122 (2017) 244506.

[12] S. Zhao, S. Butera, G. Lioliou, A.B. Krysa, A.M. Barnett, High temperature AlInP X-ray spectrometers, Sci. Rep. 9 (2019) 12155.

[13] S. Butera, G. Lioliou, A.B. Krysa, A.M. Barnett, Temperature characterisation of spectroscopic InGaP X-ray photodiodes, Nucl. Instrum. Methods Phys. Res. A 908 (2018) 277–284.

[14] S. Zhao, G. Lioliou, A.M. Barnett, Temperature dependence of commercial 4h-SiC UV Schottky photodiodes for X-ray detection and spectroscopy, Nucl. Instrum. Methods Phys. Res. A 859 (2017) 76–82.

[15] C.S. Bodie, G. Lioliou, A.M. Barnett, Hard X-ray and γ-ray spectroscopy at high temperatures using a COTS SiC photodiode, Nucl. Instrum. Methods Phys. Res. A 985 (2021) 164663.

[16] S. Zhao, G. Lioliou, S. Butera, M.D.C. Whitaker, A.M. Barnett, Electron spectroscopy with a commercial 4H-SiC photodiode, Nucl. Instrum. Methods Phys. Res. A 910 (2018) 35–40.

[17] A.A. Malafronte, A.R. Petri, J.A.C. Gonçalves, S.F. Barros, C.C. Bueno, N.L. Maidana, A. Mangiarotti, M.N. Martins, A.A. Quivy, V.R. Vanin, A low-cost small-size commercial PIN photodiode: I. Electrical characterisation and low-energy photon spectrometry, Radiat. Phys. Chem. 179 (2021) 109103.

[18] A. Mangiarotti, A.R. Petri, A.A. Malafronte, J.A.C. Gonçalves, S.F. Barros, C.C. Bueno, J.M. Fernández-Varea, N.L. Maidana, M.N. Martins, V.R. Vanin, A low-cost small-size commercial PIN photodiode: II. Comparison of measurements with monoenergetic electrons to analytical expressions and Monte Carlo simulations, accepted for publication in radiation physics and chemistry, 2021.

[19] C.C. Bueno, J.A.C. Gonçalves, R.R.de Magalhães, M.D.S. Santos, Response of PIN diodes as room temperature photon detectors, Appl. Radiat. Isot. 61 (2004) 1343–1347.

[20] C. Romei, A. Di Fulvio, C.A. Traino, R. Ciolini, F. d'Errico, Characterization of a low-cost PIN photodiode for dosimetry in diagnostic radiology, Phys. Medica 31 (2015) 112–116.

[21] C.N.P. Oliveira, H.J. Khoury, E.J.P. Santos, Pin photodiode performance comparison for dosimetry in radiology applications, Phys. Medica 32 (2016) 1495–1501.

[22] M.Y. Nikiforova, B.I. Podlepetsky, Evaluation of commercial PIN diodes as gamma radiation dosimeters, in: IOP Conference Series: Materials Science and Engineering, 498, 2019, 012015.

[23] HAMAMATSU PHOTONICS K.K., High-speed photodiodes (S5973 series: 1 GHz), Data Sheet, Cat. No. KPIN1025E10, HAMAMATSU, Hamamatsu City, 2019.

[24] C. Joseph, M. Boukadoum, J. Charlson, D. Starikov, A. Bensaoula, High-speed front end for LED-Photodiode based fluorescence lifetime measurement system, in: 2007 IEEE International Symposium on Circuits and Systems, 2007, pp. 3578-3581.

[25] Y. Katayose, et al., Development of a high dynamic range front-end electronics for the total absorption calorimeter of CALET, in: 31st International Cosmic Ray Conference, Łódź, Poland, 2009.

[26] K.K. Gan, W. Fernando, H.P. Kagan, R.D. Kass, A. Law, A. Rau, D.S. Smith, M.R.M. Lebbai, P.L. Skubic, B. Abi, F. Rizardinova, Study of the radiation hardness of VCSEL and PIN arrays, in: Proceedings of the 10th Conference, Astroparticle, Particle And Space Physics, Detectors And Medical Physics Applications, Como, Italy, 2007.

[27] T. Oka, K. Inoue, N. Yagi, Microsecond time-resolved diffraction and scattering measurements system using semi-monochromatic X-ray pulse at SPring-8 BL40XU, AIP Conf. Proc. 705 (2004) 1197–1200.

[28] G. Vízkelethy, Final Report of Sandia National Laboratories (SNL) Contribution To IAEA CRP F11016 on Utilization of Ion Accelerators for Studying and Modeling of Radiation Induced Defects in Semiconductors and Insulators, Sandia National Laboratories, New Mexico, 2016.

[29] J.H. Hubbell, S.M. Seltzer, Tables of X-Ray Mass Attenuation Coefficients and Mass Energy-Absorption Coefficients (Version 1.4), National Institute of Standards and Technology, Gaithersburg, 2004.

[30] G. Lioliou, S. Butera, A.B. Krysa, A.M. Barnett, The response of thick (10 μm) alinp x-ray and γ-ray detectors at up to 88 kev, J. Appl. Phys. (2021) in press.

[31] G. Lioliou, A.M. Barnett, Electronic noise in charge sensitive preamplifiers for x-ray spectroscopy and the benefits of a SiC input JFET, Nucl. Instrum. Methods Phys. Res. A 801 (2015) 63–72.

[32] A. Owens, Compound semiconductor radiation detectors, CRC Press, Boca Raton, 2012.

[33] C. Erd, A. Owens, G. Brammertz, M. Bavdaz, A. Peacock, V. Lämsä, S. Nenonen, H. Andersson, N. Haack, Hard X-ray test and evaluation of a prototype 32×32 pixel gallium–arsenide array, Nucl. Instrum. Methods Phys. Res. A 487 (2002) 78–89.

[34] R.H. Pehl, F.S. Goulding, D.A. Landis, M. Lenzlinger, Accurate determination of the ionization energy in semiconductor detectors, Nucl. Instrum. Methods 59 (1968) 45–55.

[35] B.G. Lowe, Measurements of Fano factors in silicon and germanium in the low-energy X-ray region, Nucl. Instrum. Methods Phys. Res. A 399 (1997) 354–364.

[36] G. Lioliou, A.M. Barnett, Prototype GaAs X-ray detector and preamplifier electronics for a deep seabed mineral XRF spectrometer, X-Ray Spectrom. 47 (2018) 201–214.

[37] G. Bertuccio, A. Pullia, A method for the determination of the noise parameters in preamplifying systems for semiconductor radiation detectors, Rev. Sci. Instrum. 64 (1993) 3294–3298.

[38] G. Bertuccio, A. Pullia, G. De Geronimo, Criteria of choice of the front-end transistor for low-noise preamplification of detector signals at sub-microsecond shaping times for X- and γ-ray spectroscopy, Nucl. Instrum. Methods Phys. Res. A 380 (1996) 301–307.

[39] G. Bertuccio, R. Casiraghi, Study of silicon carbide for X-ray detection and spectroscopy, IEEE Trans. Nucl. Sci. 50 (2003) 175–185.

[40] G. Lioliou, A.B. Krysa, A.M. Barnett, Energy response characterization of InGaP X-ray detectors, J. Appl. Phys. 124 (2018) 195704.

[41] G. Bertuccio, S. Caccia, Progress in ultra-low-noise ASICs for radiation detectors, Nucl. Instrum. Methods Phys. Res. A 579 (2007) 243–246.

[42] G. Bertuccio, R. Casiraghi, A. Cetronio, C. Lanzieri, F. Nava, Silicon carbide for high resolution X-ray detectors operating up to 100°, Nucl. Instrum. Methods Phys. Res. A 522 (2004) 413–419.

[43] C.S. Bodie, G. Lioliou, G. Lefeuvre, A.M. Barnett, A single crystal chemical vapour deposition diamond soft X-ray spectrometer, Nucl. Instrum. Methods Phys. Res. A 989 (2021) 164950.

[44] G. Bertuccio, P. Rehak, D. Xi, A novel charge sensitive preamplifier without the feedback resistor, Nucl. Instrum. Methods Phys. Res. A 326 (1993) 71–76.

[45] U. Schötzig, Half-life and X-ray emission probabilities of ^{55}Fe, Appl. Radiat. Isot. 53 (2000) 469–472.

[46] H. Xiaolong, Y. Shenggui, D. Chunsheng, Evaluation of the decay data of ^{109}Cd, Nucl. Instrum. Methods Phys. Res. A 621 (2010) 443–446.

[47] H.R. Verma, Measurements of M and L X-ray energies and relative intensities emanating from ^{241}Am source, Appl. Radiat. Isot. 122 (2017) 41–46.

[48] M.-M. Be, V. Chiste, C. Dulieu, X. Mougeot, E. Browne, V. Chechev, N. Kuzmenko, F. Kondev, A. Luca, M. Galan, A.L. Nichols, A. Arinc, X. Huang, Monographie BIPM-5, 5, 2010.

[49] G.F. Knoll, Radiation Detection and Measurements, fourth ed., John Wiley & Sons, 2010.

[50] G. Lioliou, A.M. Barnett, X-ray And γ-ray spectroscopy using a 2 × 2 gaas p^+-i-n^+ diode array, Nucl. Instrum. Methods Phys. Res. A 985 (2021) 164672.

[51] G. Lioliou, A.B. Krysa, A.M. Barnett, X-/γ- ray photon counting spectroscopy with an alinp array, Nucl. Instrum. Methods Phys. Res. A 1002 (2021) 165293.

[52] S. Butera, G. Lioliou, S. Zhao, A.B. Krysa, A.M. Barnett, Ingap 2 × 2 pixel array for x-ray and γ-ray spectroscopy, Nucl. Instrum. Methods Phys. Res. A (2021) in press.

[53] A.M. Barnett, Wide Band Gap Compound Semiconductor Detectors for X-Ray Spectroscopy in Harsh Environments, Ph.D. thesis, Department of Physics and Astronomy, University of Leicester, Leicester, UK, 2011.

[54] A.D.T. Short, An Evaluation of Gallium Arsenide for Detector Applications in X-Ray Astronomy, Ph.D. thesis, Department of Physics and Astronomy, University of Leicester, Leicester, UK, 1997.

[55] G. Lioliou, A.M. Barnett, Electron–hole pair creation and conversion efficiency in radioisotope microbatteries, Appl. Radiat. Isot. (2021) submitted for publication.
[56] S. Butera, G. Lioliou, A.B. Krysa, A.M. Barnett, Measurement of the electron–hole pair creation energy in $Al_{0.52}In_{0.48}P$ using X-ray radiation, Nucl. Instrum. Methods Phys. Res. A 879 (2017) 64–68.
[57] G. Bertuccio, D. Maiocchi, Electron–hole pair generation energy in gallium arsenide by x and γ photons, J. Appl. Phys. 92 (2002) 1248–1255.
[58] J.S. Cheong, J.S.L. Ong, J.S. Ng, A.B. Krysa, J.P.R. David, $Al_{0.52}In_{0.48}P$ SAM-APD as a blue-green detector, IEEE J. Sel. Top. Quantum Electron. 20 (2014) 142–146.
[59] I. Vurgaftman, J.R. Meyer, L.R. Ram-Mohan, Band parameters for III–V compound semiconductors and their alloys, J. Appl. Phys. 89 (2001) 5815–5875.
[60] G. Bertuccio, M. Ahangarianabhari, C. Graziani, D. Macera, Y. Shi, M. Gandola, A. Rachevski, I. Rashevskaya, A. Vacchi, G. Zampa, N. Zampa, P. Bellutti, G. Giacomini, A. Picciotto, C. Piemonte, N. Zorzi, X-ray Silicon drift detector–CMOS front-end system with high energy resolution at room temperature, IEEE Trans. Nucl. Sci. 63 (2016) 400–406.
[61] O. Madelung, Physics of Group IV Elements and III-V Compounds, Springer-Verlag, Berlin, 1982.
[62] S.K. Chaudhuri, K.J. Zavalla, K.C. Mandal, Experimental determination of electron–hole pair creation energy in 4H-SiC epitaxial layer: An absolute calibration approach, Appl. Phys. Lett. 102 (2013) 031109.
[63] A. Owens, A. Peacock, Compound semiconductor radiation detectors, Nucl. Instrum. Methods Phys. Res. A 531 (2004) 18–37.
[64] L. Rossi, P. Fischer, T. Rohe, N. Wermes, Pixel Detectors: From Fundamentals To Applications, Springer-Verlag, Berlin, 2006.